AGU PUBLICATIONS

JGR

Journal of Geophysical Research: Space Physics

RESEARCH ARTICLE
10.1002/2015JA021002

Key Points:
- Transition state with a timescale of ~10 min in the near-noon polar cap for $B_Z > 0$
- The state is consistent with the passage of old and new convection regions
- Almost simultaneous initial response in the upstream polar cap and the near noon

Correspondence to:
S. Taguchi,
taguchi@kugi.kyoto-u.ac.jp

Citation:
Taguchi, S., A. Tawara, M. R. Hairston, J. A. Slavin, G. Le, J. Matzka, and C. Stolle (2015), Response of reverse convection to fast IMF transitions, *J. Geophys. Res. Space Physics*, *120*, 4020–4037, doi:10.1002/2015JA021002.

Received 11 JAN 2015
Accepted 21 APR 2015
Accepted article online 23 APR 2015
Published online 26 MAY 2015

Response of reverse convection to fast IMF transitions

S. Taguchi[1], A. Tawara[2], M. R. Hairston[3], J. A. Slavin[4], G. Le[5], J. Matzka[6,7], and C. Stolle[6,7]

[1]Department of Geophysics, Graduate School of Science, Kyoto University, Kyoto, Japan, [2]Department of Communication Engineering and Informatics, University of Electro-Communications, Tokyo, Japan, [3]William B. Hanson Center for Space Sciences, University of Texas Dallas, Richardson, Texas, USA, [4]Department of Atmospheric, Oceanic and Space Sciences, University of Michigan, Ann Arbor, Michigan, USA, [5]NASA Goddard Space Flight Center, Greenbelt, Maryland, USA, [6]DTU Space, Technical University of Denmark, Lyngby, Denmark, [7]Now at Helmholtz Centre Potsdam, GFZ German Research Centre for Geosciences, Potsdam, Germany

Abstract The nature of the transition that high-latitude reverse convection makes in response to fast interplanetary magnetic field (IMF) changes is investigated using observations from multiple spacecraft and a ground magnetometer array. We focused on two fast IMF-transition events on 22 April 2006. Immediately after the first event, three ST5 spacecraft identified a clear change in the distribution of the polar cap field-aligned current. Coordinate observations with the Greenland magnetometer chain showed that the near-noon Hall current distribution, which is closely related to the polar cap field-aligned current or reverse convection, was in a transition state for about 10 min. For the second event, the Greenland magnetic perturbations also showed that a transition state occurred in the near-noon sector for 10–15 min. Three DMSP spacecraft that traversed the polar cap provided evidence showing that variations of the ground magnetic perturbations were produced by the transition from clockwise plasma circulation to the anticlockwise circulation over the polar cap. A simple calculation based on the Biot-Savart law shows that the near-noon transition state is consistent with the approach of a new convection region to the near-noon sector at the speed of 0.5–1 km s^{-1}, which is coupled with the moving away of the old convection region at a similar speed. For the higher-latitude sunward flow region, it is found that the convection takes a transition state almost simultaneously (within 1 min) with that in the near-noon sector, i.e., quasi-instantaneous response.

1. Introduction

The plasma convection and current in the dayside high-latitude ionosphere are directly controlled by the interplanetary magnetic field (IMF). This occurs via reconnection between the IMF and the Earth's magnetic field of the dayside magnetopause. The characteristics of those IMF-controlled convection and currents during stable IMF intervals are well understood. Transition states occur between two different stable IMF intervals. Particularly, for the southward turning from the northward IMF interval, the states have been examined extensively [e.g., *Etemadi et al.*, 1988; *Todd et al.*, 1988; *Hairston and Heelis*, 1995; *Ridley et al.*, 1998; *Ruohoniemi and Greenwald*, 1998; *Khan and Cowley*, 1999; *Huang et al.*, 2000; *Murr and Hughes*, 2001; *Nishitani et al.*, 2002; *Freeman*, 2003; *Fiori et al.*, 2012].

When the southward turning of the northward IMF occurs, reverse convection over the dayside polar cap is eventually replaced by standard two-cell convection. In reverse, for the IMF change from the southward orientation to the northward orientation, standard two-cell convection is replaced with reverse convection. For example, *Clauer and Friis-Christensen* [1988] examined the 1 min time resolution data of the ground magnetic perturbations for that IMF turning and suggested that the large-scale transition state occurs during a period of about 22 min. In either IMF turning case, standard two-cell convection is involved, and its transition state would be associated both with detailed timing of the start or stop of nightside reconnection in the near-Earth tail and dayside reconnection [*Cowley and Lockwood*, 1992].

In the present paper, we investigate the nature of a transition that is inherent to the convection driven only by dayside reconnection not involved in nightside reconnection. An ideal situation for this investigation occurred on 22 April 2006. IMF having a northward component changed very sharply twice during 1400–1500 UT on this day, and multiple spacecraft observed the polar cap immediately after both events. The first event was a northward to duskward IMF transition, and the second event was a duskward to dawnward IMF transition.

Immediately after the first IMF transition, three satellites of the polar-orbiting Space Technology 5 (ST5) mission [*Slavin et al*., 2008] passed over the dayside polar cap. Another event occurred about 30 min later. For this event, three satellites of the Defense Meteorological Satellite Program (DMSP: F13, F15, and F16) observed the polar cap. More specifically, for the first event, ST5 flew over the Kullorsuaq (KUV) station in Greenland, which was in the dayside polar cap. For the second event, DMSP spacecraft flew over Nord (NRD) in Greenland, which was in the duskside polar cap.

The Greenland magnetometer station can provide high time resolution data (20 s time resolution). Most of the past investigations for the transition state used the magnetometer data whose time resolution is 1 min or the plasma drift data obtained by the Super Dual Auroral Radar Network radars which typically have a 1–2 min time resolution. In the present study, we use 20 s time resolution magnetometer data from several Greenland magnetometer stations including the above two stations to determine the start and end times of the transition state to an accuracy of less than 1 min. Using data from multiple spacecraft together with those high time resolution data, we show the nature of the transition that high-latitude reverse convection made in response to fast IMF changes.

2. Instrumentation

The ST5 constellation orbits the Earth in a 300 km × 4500 km dawn-dusk orbit [*Slavin et al*., 2008]. The triaxial fluxgate magnetometer carried by each of the three spacecraft provides multipoint measurements of the magnetic field in the near-Earth environment. We used the magnetic perturbations obtained after subtraction of the background geomagnetic field using International Geomagnetic Reference Field [*Slavin et al*., 2008; *Wang et al*., 2009; *Le et al*., 2009]. These variations are ascribed to the passage of satellites through the field-aligned current region.

Each of the DMSP satellites (F13, F15, and F16) is in a circular orbit with an altitude of ~835 km. We used horizontal ion flow data from the ion drift meter, which measures the flow velocities perpendicular to the spacecraft's velocity vector [*Greenspan et al*., 1988]. The satellite pass is roughly parallel to the dawn-dusk meridian in magnetic local time (MLT)-magnetic latitude (MLAT) coordinate, and one horizontal component perpendicular to the satellite track can be used to determine which part of the dayside polar cap convection has a sunward component. This is a key feature of the convection associated with the northward IMF.

The Greenland magnetometer array (operated by DTU Space, Technical University of Denmark) consists of a West Coast Chain with 13 stations and an East Coast Chain with five stations. The data from this magnetometer array are very useful for understanding the temporal variations of polar cap phenomena [e.g., *Friis-Christensen et al*., 1988]. ST5 flew over the KUV station of the West Coast Chain during one of the two events dealt with in this paper. For another event, DMSP spacecraft flew over NRD of the East Coast Chain. In addition to the data from these two magnetometer stations, we used the data from four more stations from the West Coast Chain (i.e., Qaanaaq (formerly Thule: THL), Savissivik: SVS, Upernavik: UPN, and Uummannaq: UMQ). For the East Coast Chain, the data from Danmarkshaven (DMH) were also used. The detailed position of these seven stations in MLT-MLAT coordinates will be described in section 4.2.

3. Dayside Polar Cap Current System Associated With Reverse Convection

Reverse convection accompanies field-aligned currents over the polar cap. A basic mode of the polar cap field-aligned current is a pair current system consisting of a current flowing out of the prenoon polar cap and a current flowing into the postnoon polar cap [e.g., *Araki et al*., 1984; *Iijima et al*., 1984]. In Figure 1, we show the illustration of that simplified current system, including some related phenomena. A map of Greenland and its neighboring area is included. Solid gray arrows indicate the field-aligned currents. We assume that the field-aligned current flows in or out of a circular area. The dashed gray arrows represent parts of their closure current in the *E* region, i.e., the Pedersen current. Note that the part of the Pedersen current is shown in this picture for simplicity.

When the height-integrated ionospheric conductivity is assumed to be spatially uniform, which is reasonable for the dayside polar cap ionosphere, the current continuity between the field-aligned current and the

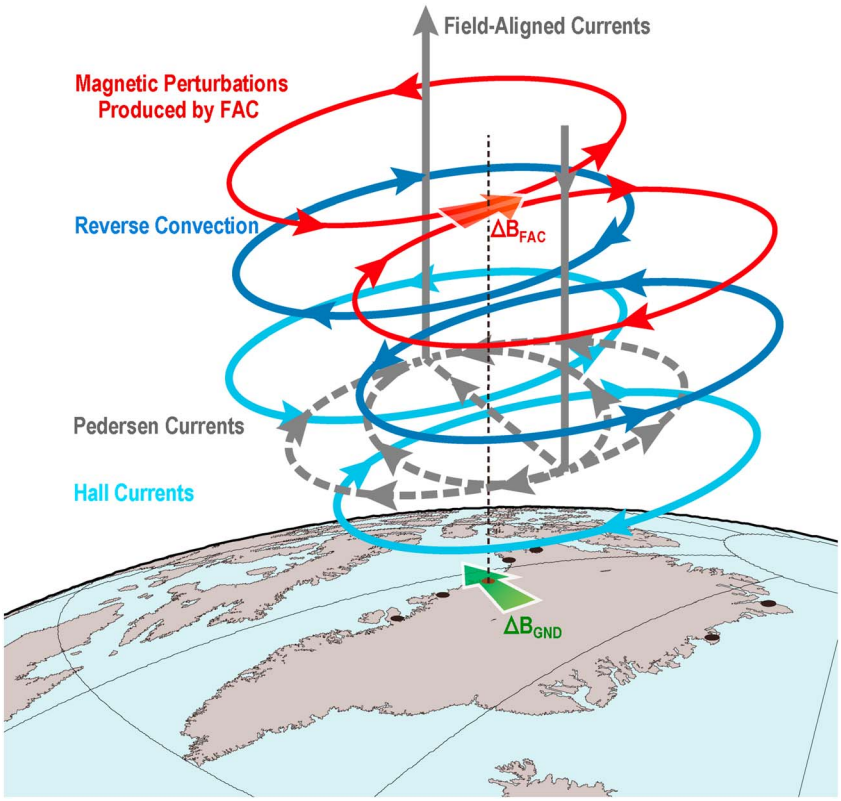

Figure 1. Illustration of the simplified current system in the polar cap during northward IMF including some related phenomena. A map of the Greenland and its neighboring area is included. Solid gray arrows indicate the field-aligned currents and their closure current in the *E* region, i.e., the Pedersen current. Part of the Pedersen current is shown for simplicity. The blue circles show the reverse convection, while the associated Hall current is indicated by the light blue circles. The green arrow denoted ΔB_{GND} represents the predominant direction of the ground magnetic perturbations beneath the center of the sunward flow region of the reverse convection. The red circles around the field-aligned current represent magnetic perturbations produced by the field-aligned current. The magnetic perturbations pointing north, which are collocated with the southward (or sunward) flow region of the reverse convection, are denoted ΔB_{FAC}.

closure current can be described by the following relation using the height-integrated Pedersen conductivity (Σ_P) and the horizontal divergence of the electric field $\nabla_\perp \cdot \boldsymbol{E}$:

$$j_{//} = \Sigma_P \nabla_\perp \cdot \boldsymbol{E} \tag{1}$$

where $j_{//}$ is the field-aligned current density, which is positive for the current into the ionosphere.

Reverse convection that is driven by $\boldsymbol{E}$ is indicated by two blue circles in Figure 1. The light blue circles, shown just below the blue circles, represent the Hall current associated with the reverse convection. With the assumption of uniform conductivities and vertical field-aligned currents, the Hall current is the only current system that produces ground magnetic perturbations because the magnetic perturbations of the field-aligned current cancels that of the Pedersen current [*Fukushima*, 1969]. The green arrow, denoted ΔB_{GND} in Figure 1, represents the predominant direction of the ground magnetic perturbations beneath the center of the sunward flow region of the reverse convection. The perturbation is oriented westward because the Hall current is flowing northward in the ionosphere closest to that point.

In Figure 1, the two red circles represent magnetic perturbations produced by the field-aligned current. As is shown later, this sort of the magnetic perturbation was actually observed by ST5. The magnetic perturbations pointing north, which are collocated with the southward (or sunward) flow region of the reverse convection, are denoted ΔB_{FAC}. Beneath these northward magnetic field perturbations, there occur ground magnetic

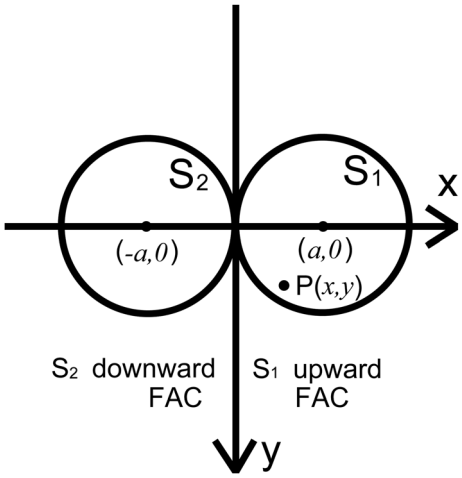

Figure 2. Horizontal cross section of an idealized polar cap field-aligned current distribution in which the twin homogeneous cylindrical current is flowing vertically. The *x* axis represents the direction parallel to the dawn-dusk meridian, while the *y* axis shows the direction parallel to the noon-midnight meridian. S_1 and S_2 represent the upward and downward field-aligned current regions, respectively. $P(x, y)$ is an arbitrary point in S_1.

perturbations oriented westward (as is represented by ΔB_{GND}). As was mentioned earlier, the ground magnetic perturbations are created by the Hall current (light blue circles). The relation between the westward magnetic perturbations on the ground and the northward magnetic perturbations in space will be used in section 4.2.

Before describing the horizontal distribution of the magnetic perturbations produced by the polar cap field-aligned currents in detail, we briefly consider a simple case where the field-aligned current is assumed to be extending in an infinite homogenous sheet. The magnetic perturbations produced by the infinite sheet have a linear relation with the orthogonal electric field variations. This can be obtained through Ampère's law and equation (1) under the infinite current sheet approximation; and in fact, DE2 satellite observations showed that these two parameters are highly correlated [*Sugiura et al.*, 1982; *Ishii et al.*, 1992]. Taking the direction of the electric field and that of the magnetic perturbation as *x* and *y* direction, respectively, E_x and δB_y can be related as follows:

$$\Sigma_P E_x = \frac{\delta B_y}{\mu_0} \tag{2}$$

where μ_0 is the magnetic permeability in vacuum. Taking the vertical Earth's main field to be $\boldsymbol{B} = B_0 \mathbf{e}_z$, we obtain the $E \times B$ drift from the vector product of the electric field (*x* direction) and the Earth's main field (*z* direction). The $E \times B$ drift can be described from equation (2) as follows:

$$v_y = -\frac{1}{\mu_0 \Sigma_P B_0} \delta B_y \tag{3}$$

where v_y is the velocity of the $E \times B$ drift. Equation (3) states that the drift velocity is antiparallel to the magnetic perturbation created by the field-aligned current in the Northern Hemisphere. This relation has been used by *Taguchi et al.* [1993] for deducing the plasma convection pattern in the dayside cusp field-aligned current region. Note that for the southern ionosphere, the drift velocity and magnetic perturbation are parallel.

We now consider a situation for the polar cap field-aligned current, which flows in or out of a more or less circular area of the polar cap. Figure 2 represents the horizontal cross section of an idealized field-aligned current distribution in which the twin homogeneous cylindrical current is flowing vertically. In a manner similar to the case for the infinite sheet current described above, we assume that the cylindrical current system is a static structure. This assumption may be a zeroth order approximation for the present ST5 field-aligned current observation. We will show later that a quasi-symmetrical twin-current system changes to an asymmetrical twin-current system during roughly 10 min in response to fast IMF transition. Neither the homogeneity of the current nor the time independence of the structure is assured. A higher-order approximation needs to be studied in the future.

In Figure 2, the *x* axis represents the direction parallel to the dawn-dusk meridian, while the *y* axis shows the direction parallel to the noon-midnight meridian. S_1 and S_2 represent the upward and downward field-aligned current regions, respectively. $P(x, y)$ is an arbitrary point in S_1. The direction of the Earth's main field is the positive *z* direction. The circular cross section of each field-aligned current has a radius of *a*, and the current in that region has a constant density of $j_{//}$. We apply the Ampère's law

$$\oint_C \delta \boldsymbol{B} \cdot d\boldsymbol{l} = \mu_0 \int_S \boldsymbol{j} \cdot \boldsymbol{n} dS \tag{4}$$

where $\delta\boldsymbol{B}$, $\boldsymbol{j}$, and $\boldsymbol{n}$ are the magnetic perturbation, the current density, and the normal vector of the surface of the volume, respectively, for a single cylindrical current region, we can obtain the magnitude of the magnetic perturbation at a distance of r as follows:

$$\delta B_\varphi = \frac{\mu_0 j_{//} r}{2} \quad (r \le a) \tag{5}$$

$$\delta B_\varphi = \frac{\mu_0 j_{//} a^2}{2r} \quad (r > a) \tag{6}$$

where δB_φ represents that the magnetic perturbation has the only azimuthal component. Applying equations (5) and (6) for the twin cylindrical current shown in Figure 2, the magnetic perturbations at $P(x, y)$ in S_1 is given in the Cartesian coordinate system as follows:

$$\delta B_x = \frac{\mu_0 j_{//}}{2}\left\{ y - \frac{a^2 y}{(x+a)^2 + y^2} \right\} \tag{7}$$

$$\delta B_y = -\frac{\mu_0 j_{//}}{2}\left\{ (x-a) - \frac{a^2 (x+a)}{(x+a)^2 + y^2} \right\} \tag{8}$$

In both (7) and (8), the first term is the contribution from S_1 itself, while the second term, shown in a fractional form, comes from S_2. For example, for $P = (0, 0)$, which is the contact point of these two current regions, $(\delta B_x, \delta B_y) = (0, \mu_0 j_{//} a)$. The magnetic perturbations are oriented toward the positive y, i.e., northward, as has been shown by ΔB_{FAC} in Figure 1.

To obtain the electric field, we consider a single cylindrical current region again. By integrating equation (1) and using Gauss's integral theorem, we obtain the following equation:

$$\oint_S \boldsymbol{E} \cdot \boldsymbol{n} \mathrm{d}S = \int_V \frac{j_{//}}{\Sigma_P} \mathrm{d}V \tag{9}$$

By applying equation (9) to the cylindrical volume whose radius is r, we can obtain the magnitude of the radial electric field:

$$E_r = \frac{j_{//}}{2\Sigma_P} \mathrm{r} \quad (r \le a) \tag{10}$$

$$E_r = \frac{j_{//} a^2}{2\Sigma_P r} \quad (r > a) \tag{11}$$

Equations (5), (6), (10), and (11) show that the ratio of the magnitude of the electric field to that of the orthogonal magnetic perturbation is $(\mu_0 \Sigma_P)^{-1}$ at an arbitrary distance from the center of a single cylindrical current region.

From the requirement of the downward Poynting vector, i.e., $\boldsymbol{E} \times \delta\boldsymbol{B}/\mu_0 = k\boldsymbol{e}_Z$ $(k > 0)$, we find that the radial electric field vector $\boldsymbol{E}$ is in the direction of $\delta\boldsymbol{B} \times \boldsymbol{e}_Z$. The relation between the electric field vector and the magnetic perturbation vector is expressed as

$$\boldsymbol{E} = (\mu_0 \Sigma_P)^{-1} \delta\boldsymbol{B} \times \boldsymbol{e}_Z \tag{12}$$

In the twin cylindrical current, which is shown in Figure 2, the electric field at P inside S_1 consists of the dominant contribution from S_1 itself, which is represented by equation (10), and the minor contribution from S_2, which is represented by equation (11). Either contribution has the same linear relation with the orthogonal magnetic perturbations as noted above. The specific expression of the E_x and E_y components can be easily obtained from equations (7), (8), and (12). We find that in the twin homogeneous cylindrical current, the $E \times B$ drift vector, $\boldsymbol{v}$ $(= \boldsymbol{E} \times \boldsymbol{e}_z / B_0)$, satisfies the following relation:

$$\boldsymbol{v} = -\frac{1}{\mu_0 \Sigma_P B_0} \delta\boldsymbol{B} \tag{13}$$

This is a generalized form of equation (3). The magnetic perturbations caused by the polar cap twin-field-aligned current system in the Northern Hemisphere can be antiparallel to the $E \times B$ drift. This relation will

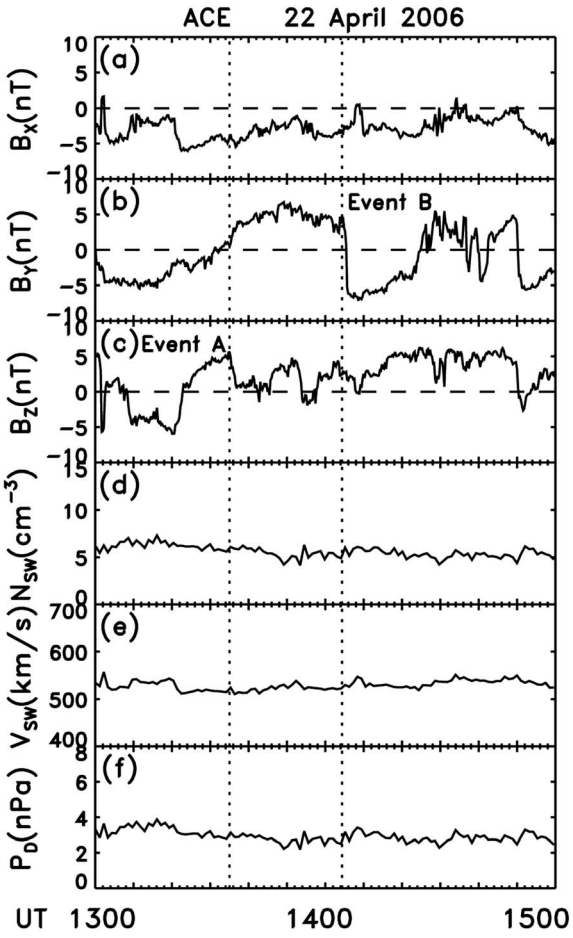

Figure 3. ACE solar wind conditions from 1300 to 1500 UT on 22 April 2006. The (a) *X*, (b) *Y*, and (c) *Z* components of the IMF in the GSM coordinate, the (d) solar wind proton density, (e) the flow speed, and the (f) dynamic pressure are plotted. The two dotted lines indicate the start time of the two fast IMF-transition events.

be used for the plot of the ST5 magnetic field data in section 4.2. For $|\delta \boldsymbol{B}| = 300$ nT, for example, $|\boldsymbol{v}|$ is roughly 1 km s^{-1} when we take Σ_p and B_0 to be 5 S and 50,000 nT, respectively.

4. Observations

4.1. Solar Wind

Figure 3 shows the solar wind data obtained by the ACE spacecraft from 1300 to 1500 UT on 22 April 2006. No time lag is considered in this plot. After approximately 1322 UT, IMF B_Z was predominantly positive (Figure 3c). The two dotted lines drawn in that positive B_Z interval (specifically at 1335:02 and 1404:22 UT) indicate the start time of the two fast IMF-transition events. In Event A, the 16 s average IMF data show that (B_Y, B_Z) changed from approximately (0.5, 5.6) to (3.3, 0.5) nT during 112 s. In other words, the purely northward IMF tilted duskward rapidly. In Event B, IMF (B_Y, B_Z) = (4.7, 2.4) nT at 1404:22 UT sharply changed to (−5.3, 1.7) nT during 80 s. The duskward IMF changed to the dawnward IMF very quickly.

The *X* component of IMF, B_X, was clearly negative during these two brief periods (Figure 3a), and its magnitude was comparable to the magnitude of B_Z (Figure 3c), indicating a favorable condition for lobe reconnection poleward of the northern cusp [e.g., *Luhmann et al.*, 1984; *Knipp et al.*, 1993; *Taguchi and Hoffman*, 1995, 1996]. Solar wind plasma parameters were relatively stable (Figures 3d–3f). The solar wind plasma density, N_{sw}, was 5 to 6 cm^{-3} around both events (Figure 3d). The solar wind speed was approximately constant at 520 km s^{-1} (Figure 3e). The dynamic pressure was around 3 nPa for both events (Figure 3f). There was no large enhancement/depression in the dynamic pressure around the times of both events, although a small enhancement (~0.5 nPa) accompanied Event B. This stability of the dynamic pressure indicates that the prominent variations in the ground magnetic perturbation, which will be shown later, are not phenomena related to sudden commencements.

4.2. Transition State Triggered by Event A and ST5 Observations

Figure 4 shows the ground magnetic perturbations observed at KUV during 14:00–15:20 UT, together with IMF data obtained in the magnetosheath by Cluster C2 [*Balogh et al.*, 2001; *Laakso et al.*, 2010] and the *AL* index. The dotted lines indicate the presumed signatures of Event A and Event B which were defined in the ACE data (Figure 3). We also refer to these magnetic field changes defined in the Cluster data (Figure 4) as Event A and Event B for simplicity. The Cluster C2 was located at (X_{GSM}, Y_{GSM}, Z_{GSM}) = (2.82, −6.69, −12.93) R_E and (2.46, −0.08, −12.95) R_E at 1423 UT (Event A), and at 1453 UT (Event B), respectively. The B_Y and B_Z components of the Cluster magnetic field were larger than those of the ACE magnetic field observed in the upstream solar wind (Figure 3) by a factor of roughly 3, indicating that Cluster C2 was in the magnetosheath. The green and red vertical lines shown at 1426:40 UT and at 1437:45 UT just after Event A represent the times of the passage of ST5 (leading (ST5-A) and trailing (ST5-C) spacecraft,

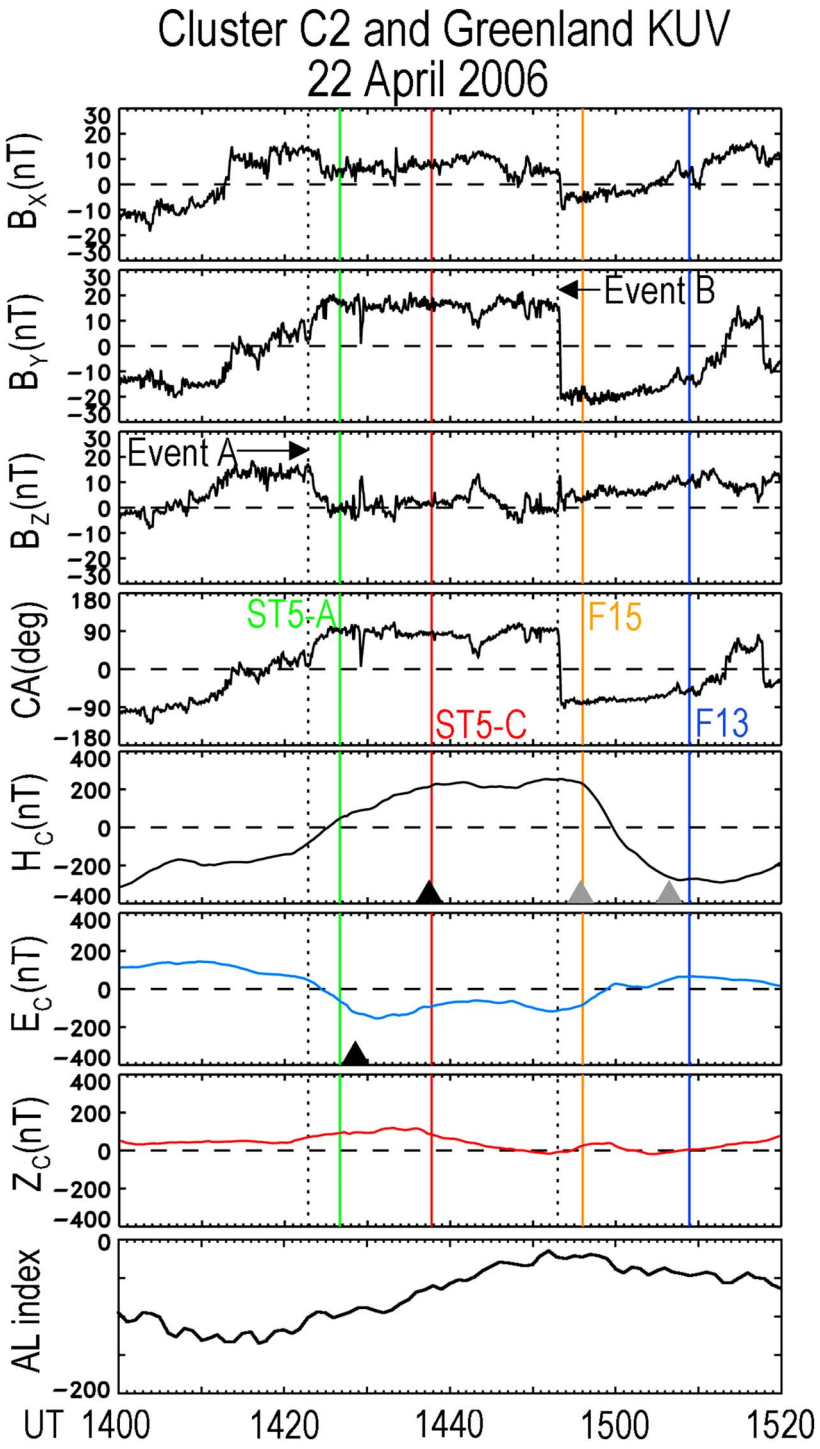

Figure 4. Ground magnetic perturbations observed at KUV during 14:00–15:20 UT, together with IMF data obtained in the near-Earth magnetosheath by Cluster C2 spacecraft and the *AL* index. (first panel–fourth panel) The *X*, *Y*, and *Z* components of the magnetosheath IMF in the GSM coordinate and the clock angle (CA). (fifth panel–eighth panel) The three components (H_C, E_C, and Z_C) of the ground magnetic perturbations (20 s time resolution) and the *AL* index. The green and red vertical lines represent the times of the passage of ST5 (ST5-A and ST5-C, respectively) over KUV, while the orange and blue vertical lines indicate the times of observation by DMSP F15 and F13, respectively. The black triangle in the E_C component (Figure 4, sixth panel) indicates the time when the ground magnetic perturbation deviated most westward. The black triangle in the H_C (Figure 4, fifth panel) is the time when the H_C component became stable after its increase. The two gray triangles in the H_C component (Figure 4, fifth panel) represent the start and end times of the characteristic variation that occurred immediately after Event B.

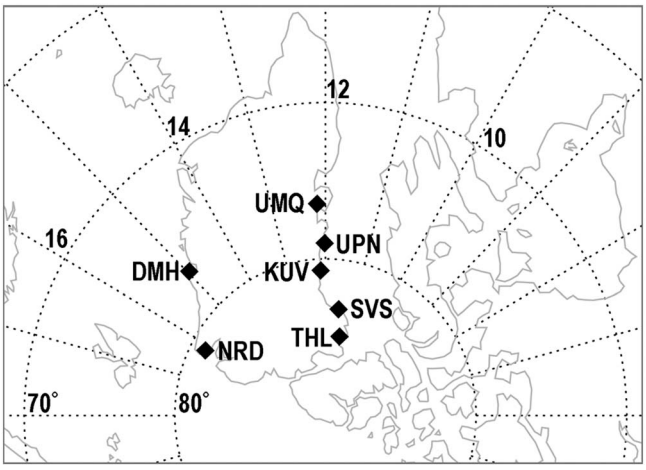

Figure 5. Location of the seven stations of the Greenland magnetometer array, whose data are used in this study.

respectively) over KUV, while the orange and blue vertical lines after Event B indicate the times of observation by DMSP F15 and F13, respectively.

The magnitude of the *AL* index (Figure 4, eighth panel) during the plotted interval is mostly less than 100 nT. These small values indicate that there were no substorm activities in spite of the fact that a brief southward IMF excursion occurred a couple of times between Event A and Event B (see also Figure 3c). This means that the convection or current dealt with in this paper is not involved in nightside reconnection. The H_C, E_C, and Z_C components (20 s time resolution) of the ground magnetic perturbations at KUV, which are shown above the *AL* index panel, represent the northward, eastward, and downward components in the corrected geomagnetic coordinate system, respectively. These components were obtained through the transformation of the perturbation vectors expressed in the local magnetic coordinate system.

The black triangle in the E_C component in Figure 4 indicated 1428:30 UT, (i.e., the time when the ground magnetic perturbation deviated most westward during the plotted interval). The E_C component decreased slightly after 1428:30 UT, but those magnetic perturbations were less westward than that at 1428:30 UT since the H_C component increased. The direction of the magnetic perturbations at that time was approximately 57° west of north in the corrected geomagnetic coordinate system. This angle will be used in section 5. As was shown in Figure 1, the westward magnetic perturbations on the ground suggest that the flow had a sunward component in the ionosphere directly above that point. At the time of this observation, KUV was located approximately at 1200 MLT. The westward deviation of the ground magnetic perturbation appears to reflect the situation in which the direction of the IMF was closest to north, i.e., the start of Event A. The time of Event A at Cluster C2 was approximately 1422:50 UT, which was 5 min 40 s earlier than 1428:30 UT, when the ground magnetic perturbation deviated most westward.

The black triangle in the H_C in Figure 4 shows the time when the H_C component became stable after its increase. For the determination of this time, we first compared the H_C component at each time (after 1430 UT) with the average H_C value from the following 10 min and took the first point when the former exceeded 95% of the latter. The direction of the magnetic perturbations at this time (1437:30 UT) was approximately 24° west from north in the corrected geomagnetic coordinate system.

The increase in the H_C component suggests that westward flow strengthens. Since the westward flow (i.e., flow toward the prenoon side) is produced by reconnection for IMF $B_Y > 0$, the start of the increase in the H_C component is consistent with the IMF change to $B_Y > 0$ from $B_Y \sim 0$ (i.e., Event A). We then determined the duration of the magnetic variation between the times shown within the two black triangles as a transition state triggered by Event A. The duration of the defined transition state at KUV was 9 min.

The two gray colored triangles in the H_C component in Figure 4 represent the start and end times of the characteristic variation that occurred immediately after Event B. The details of the variation will be described in section 4.3. The magnetic perturbation at the start and end times was oriented approximately 20° west from north, and 11° east from south, respectively. These angles will be used in section 5.

Figure 5 shows the location of the seven ground magnetic stations (including KUV) at 1426 UT in the corrected geomagnetic coordinate system. As noted above, KUV is located at about 1200 MLT. The other four stations from the West Coast Chain were also similarly located in the noon sector. DMH and NRD from the East Coast Chain were located at ~1500 MLT and ~1600 MLT, respectively.

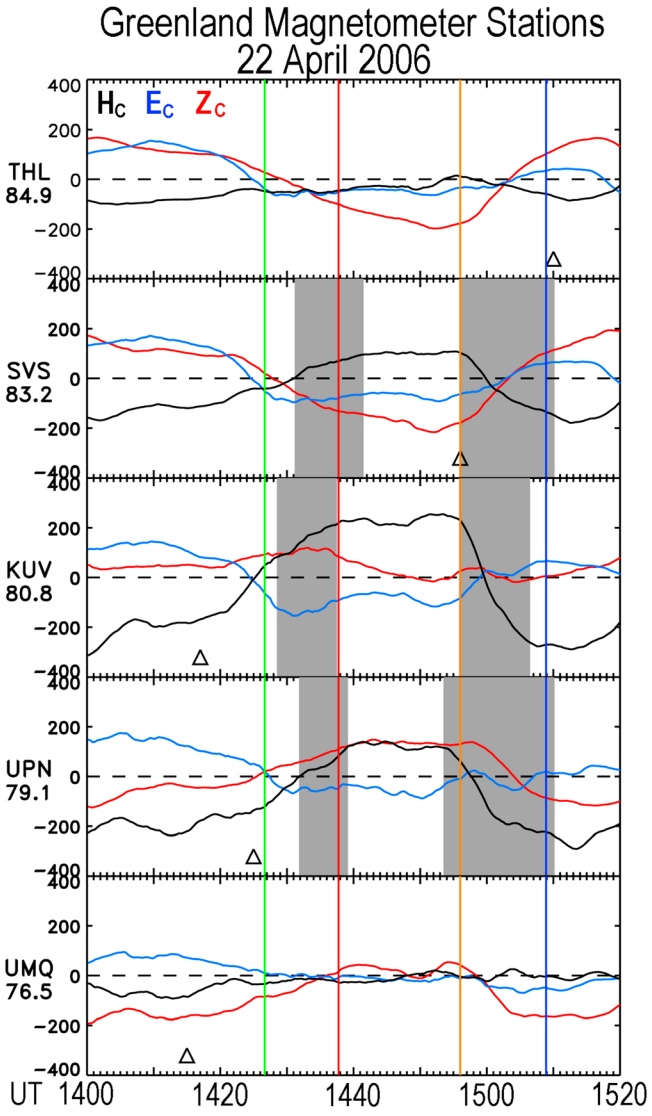

Figure 6. Ground magnetic perturbations observed at the five stations of the West Coast Chain during 1400–1520 UT (same interval as that in Figure 4). In each of the panels, the data shown in black, blue, and red are the H_C, E_C, and Z_C components of the ground magnetic perturbations, respectively. The open triangle indicates 1200 MLT for each station. The interval indicated by a gray box in the panel for SVS, KUV, and UPN represents the duration of a transition state determined using the same method used in Figure 4. The four vertical lines are also the same as those shown in Figure 4.

The ground magnetic perturbations observed at the five stations of the West Coast Chain during 1400–1520 UT (same interval as that in Figure 4) are shown in Figure 6. In each of the panels of Figure 6, the H_C, E_C, and Z_C components of the ground magnetic perturbations are shown in black, blue, and red, respectively. The third panel shows the data from KUV, which are the same as those shown in Figure 4. The four vertical lines in the panels are also the same as those shown in Figure 4. The corrected geomagnetic latitude of each station is indicated on the left side of each panel.

The interval indicated by a gray box in the panel for SVS, KUV, and UPN represents the duration of a transition state determined using the same method used for the KUV data in Figure 4. The start times from SVS, KUV, and UPN were 1431:10, 1428:30, and 1431:50 UT, respectively. This similarity strengthens the hypothesis that flow having a sunward component was present around 80° MLAT at the near-noon meridian at this time. Similar magnetic variations were not seen at UMQ (Figure 6, bottom), which is located at 76.5° MLAT.

We also defined the end of the transition state (i.e., the end of the interval indicated by the gray box) in a manner similar to the method used for the KUV data (Figure 4). The end times from the three stations were similar, 1441:30 UT for SVS, 1437:30 UT for KUV, and 1439:10 UT for UPN. The duration for the transition state determined at SVS, KUV, and UPN is 10 min 20 s, 9 min, and 7 min 20 s, respectively. The duration of the defined transition state was roughly 10 min. The second gray box in each panel is for the transition state of Event B, which will be described later.

The main panel of Figure 7 shows the data from the ST5 spacecraft, and the inset shows the direction of the plasma flow, which was inferred from ground magnetic perturbations at UPN, KUV, and SVS. The green colored vectors in the inset represent the direction of the plasma flow, which were obtained from the H_C and E_C components of the ground magnetic perturbation at 1426:30 UT. This time was immediately before the start of the transition state (the start of the first gray colored interval in Figure 6). The red vectors in the inset of Figure 7 are from the magnetic perturbations at 1437:30 UT, which was almost the same as the time when the transition state at KUV ended. From the direction of these arrows, we can infer that the flow toward the prenoon side occupied the near-noon sector at the end of the transition state.

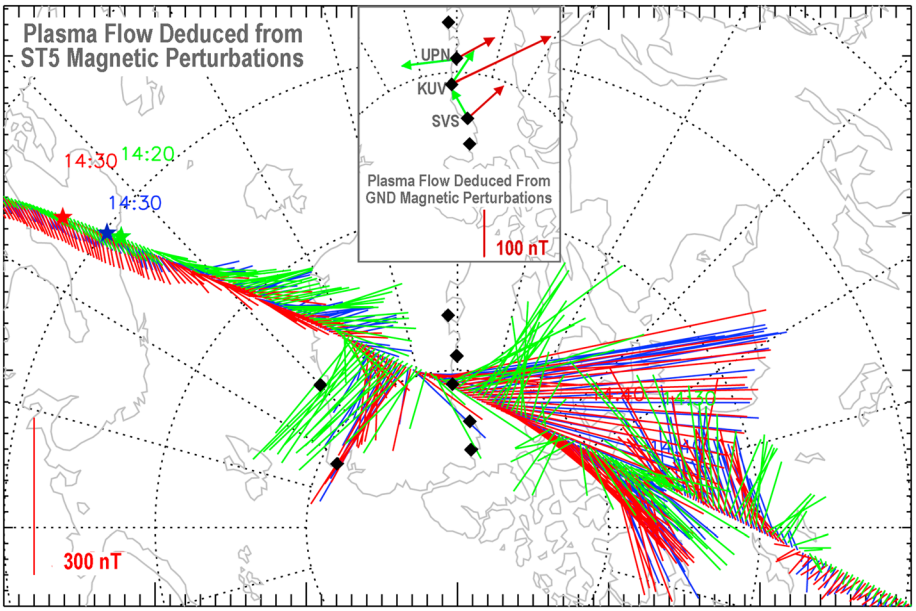

Figure 7. Data from the ST5 spacecraft (main panel) and data from the ground magnetometers at UPN, KUV, and SVS (inset). The green colored vectors in the inset represent the direction of the inferred plasma flow, which were obtained from the H_C and E_C components of the ground magnetic perturbation at 1426:30 UT (the time indicated by the green line in Figures 4 and 6). The red vectors in the inset are from the magnetic perturbations at 1437:30 UT. In the main panel, data from ST5 are shown with a vector that is antiparallel to the observed magnetic perturbation. The green vectors show the data obtained by the leading ST5 spacecraft (ST5-A). The data obtained by the middle (ST5-094 or ST5-B) and trailing spacecraft (ST5-224 or ST5-C) are plotted in blue and red, respectively. Three star symbols along the passes indicate the location of the satellite at a given time.

The ST5 spacecraft observation provides evidence for this inference. Data from the ST5 spacecraft are shown with a vector that is antiparallel to the observed magnetic perturbation. When equation (13) is valid, the plotted vector would be parallel to the $E \times B$ drift. The length of the plotted vector simply represents the magnitude of the magnetic perturbation itself and does not consider the coefficient of the right-handed term of equation (13), $(\mu_0 \Sigma_P B_0)^{-1}$. The scale is given in the bottom left of Figure 7. As noted in section 3, the magnitude of 300 nT represents roughly 1 km s^{-1}.

The green vectors show the data obtained by the leading ST5 spacecraft (ST5-155 or ST5-A). It flew over KUV at 1426:40 UT (green line in Figures 4 and 6). The data obtained by the middle (ST5-094 or ST5-B) and trailing spacecraft (ST5-224 or ST5-C) are plotted in blue and red, respectively. The trailing spacecraft flew over KUV at 1437:45 UT (red vertical line in Figures 4 and 6), roughly 11 min later than the leading satellite. The middle spacecraft was flying just 1 min ahead of the trailing satellite. The data from the middle spacecraft were not substantially different from those obtained by the trailing satellite. Three star symbols along the passes (top left in Figure 7) indicate the location of the satellite at a given time.

A clear difference was found between the green vectors and the red (or blue) vectors. The green vectors had sunward and westward components above KUV, and those vectors are central parts of the twin reverse convection system in the dayside polar cap. The red vectors give evidence demonstrating that the pattern of the reverse convection was deformed so that the central flow, which had sunward and westward components, shifted predominantly westward.

For the deduced flow shown in the inset, we note that among the three stations the westward flow (red arrow) was strongest at KUV. This means that the strongest Hall current toward the postnoon side (i.e., the eastward current) occurred near that latitude. In this situation, magnetic perturbations should have an upward (i.e., a negative Z_C) component as well as a northward (i.e., a positive) H_C component on the poleward side of that latitude. This is consistent with the magnetic perturbations obtained at THL and SVS (Figure 6). Similarly, the magnetic perturbations had a positive Z_C component on the equatorward side of that latitude, as is seen in the data from UPN (Figure 6).

4.3. Transition State Triggered by Event B and DMSP Observations

The transition state defined for Event B is indicated by the second gray box in each of three panels for the SVS, KUV, and UPN data in Figure 6. As the start of the transition state, we took the time when the H_C component became less than the average H_C component during the preceding 10 min and was followed by the decrease of more than 10 nT during 1 min. The decrease of $>$10 nT for 1 min has been used as a significant variation by *Taguchi et al.* [1997]. The start times at the three stations were very similar.

The end of the transition state was determined in a manner similar to that for the end time of the transition state for Event A. The duration of the defined transition state was 14 min, 10 min 40 s, and 16 min 40 s at SVS, KUV, and UPN, respectively. The H_C component reversed during the transition, and the dominant direction of the magnetic perturbation became southward. The Z_C component at THL and SVS changed from negative to positive. These suggest that the clockwise convection (red vectors in Figure 7) changed to anticlockwise convection.

Evidence for this change was provided by observations of DMSP ion drift. Figures 8a and 8b show the DMSP ion drift data near the start and end of the transition state, respectively. In Figure 8a, the ion drift from DMSP F15 and F16 is plotted. We show the satellite position at 1456:00 UT for each pass. The F15 and F16 data obtained before this time are indicated by orange and green, respectively. We know from these vectors that clockwise convection was dominant before the start of the transition state.

Figure 8b shows the ion drift data from DMSP F13 (blue), which were mostly obtained after the end of the transition state. For comparison, we also include the ion drift data from DMSP F15 (the same as the F15 data in Figure 8a). We know from their comparison that the clockwise convection changed direction to anticlockwise. The position of DMSP F13 at 1508:54 UT is indicated in Figure 8b (near 1700 MLT). The observation at this time provided evidence that the flow became antisunward by, at the latest, ~13 min (= 1508:54 UT–1456 UT) after the start of the near-noon transition state.

To understand when the initial response occurred over the duskside polar cap, we examined the ground magnetic perturbations observed at DMH and NRD. Figure 9 shows the ground magnetic perturbations observed at these stations (second and third panels) and their comparison to the data obtained at KUV (also shown in Figures 4 and 6). The vertical gray line in each of the panels for DMH and NRD shows the time that was determined using the similar method as that used for the determination of the KUV transition state (Figure 6). The gray line in the KUV panel shows the time determined in Figure 6. The three start times from the different MLT regions were within 1 min and very close. This indicates that the clockwise reverse convection responds almost simultaneously at the very beginning of the transition state in the near-noon sector and in the upstream part of the sunward flow (on the duskside). The orange line shows the time when DMSP F15 passed directly above NRD, which is discussed below.

We know from Figures 8a and 8b that the DMSP F15 ion drift had a sunward component in the ionosphere above NRD. This strongly suggests that the positive H_C component detected at NRD at this time (Figure 9, third panel) was produced by the Hall current with an antisunward component. Antisunward current in the dusk polar cap had an eastward component. Since the eastward current produces the northward magnetic perturbations on the ground, the decrease in the northward component after approximately 1456 UT (Figure 9, third panel) would be due to the decrease in the strength of the eastward current (i.e., the flow having a sunward component). Involvement of conductivity in this decrease will be ruled out, in the present case, based upon precipitating-particle data from DMSP F15, shown below.

Figure 10 shows data from the DMSP F15 particle spectrometers that measure precipitating electrons and ions with energies between 30 eV and 30 keV once per second [*Hardy et al.*, 1984]. The energy fluxes of the electrons and ions were plotted for the interval 1446–1504 UT, with color codes in Figure 10 (third and fourth panels), along with the ion and electron integral energy flux and average energy. Note that the ion-energy scale is inverted in Figure 10, fourth panel. The orange line in Figure 10 (third panel) (precipitating electron data) represents the time when DMSP F15 passed directly above NRD. No high-energy precipitation occurred around this time, suggesting that the conductivity in this region was not created by the high-energy particle precipitation. This means that a sudden decrease in the conductivity should not occur in the present case.

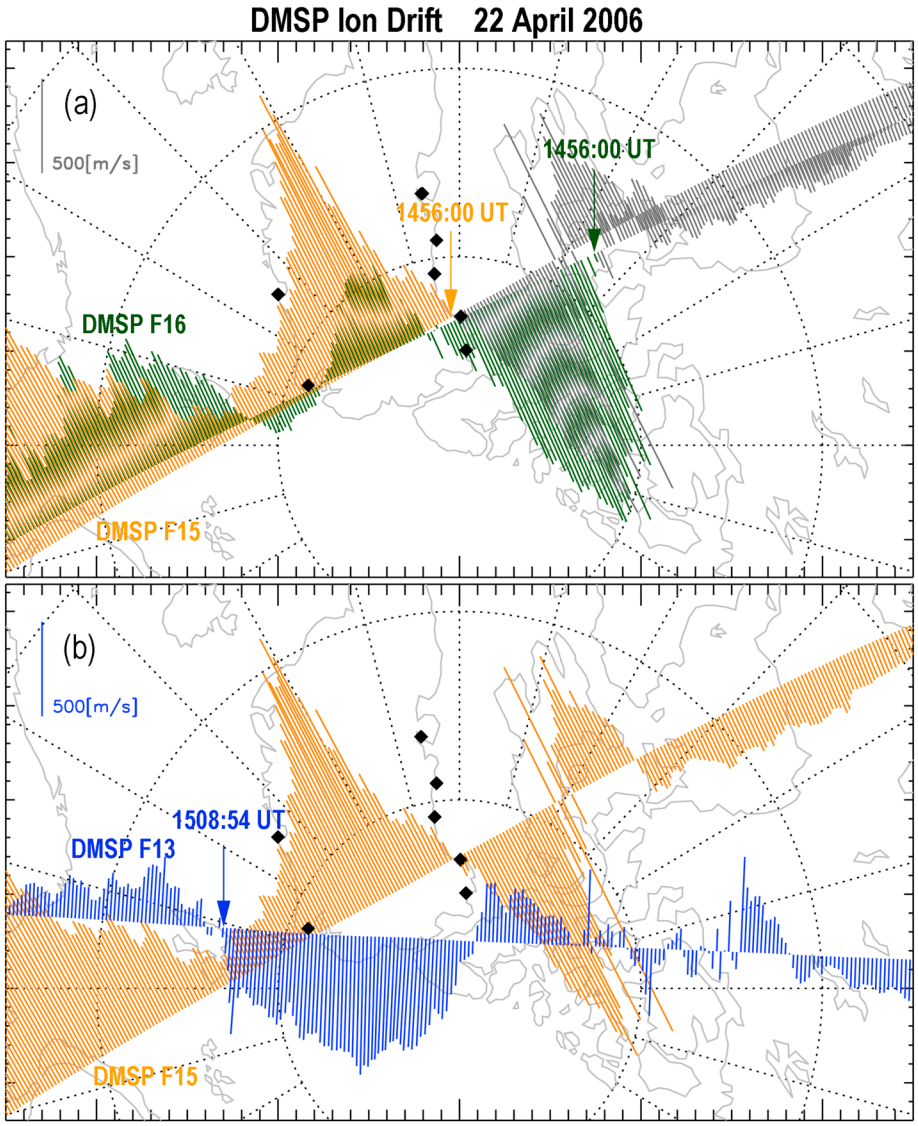

Figure 8. Ion drift data from (a) DMSP F15 (orange) and DMSP F16 (green) near the start of the transition state for Event B, and those from (b) DMSP F13 (blue) near the end of the transition state, together with their comparison with those from DMSP F15. In Figure 8a, the data after 1456:00 UT are shown in gray.

5. Discussion

5.1. Simultaneous Response in the Near-Noon and Upstream Part of Sunward Flow

We have suggested in Figure 9 that the clockwise reverse convection responds almost simultaneously (within 1 min) at the very beginning of the transition state in the near-noon sector and in the upstream part of the sunward flow (on the duskside). In principle, a magnetometer located far away from noon could respond to currents localized to the near-noon sector. The magnetic perturbations observed at KUV in the near-noon sector indicate that the H_C component decreased by 39 nT during 1 min just after the start of the transition state (Figures 4 and 6). On the other hand, the corresponding decreases in the H_C component at DMH and NRD was about 10 nT and 11 nT, respectively. These magnitudes are smaller than that from the near-noon sector, but considering that these stations are roughly 1000 km away from noon (about 10 times the distance to the above *E* region or ~115 km), the variations at DMH and NRD will not be ascribed to the near-noon current. We need to consider a mode of response that is proper to the upstream part of the sunward flow.

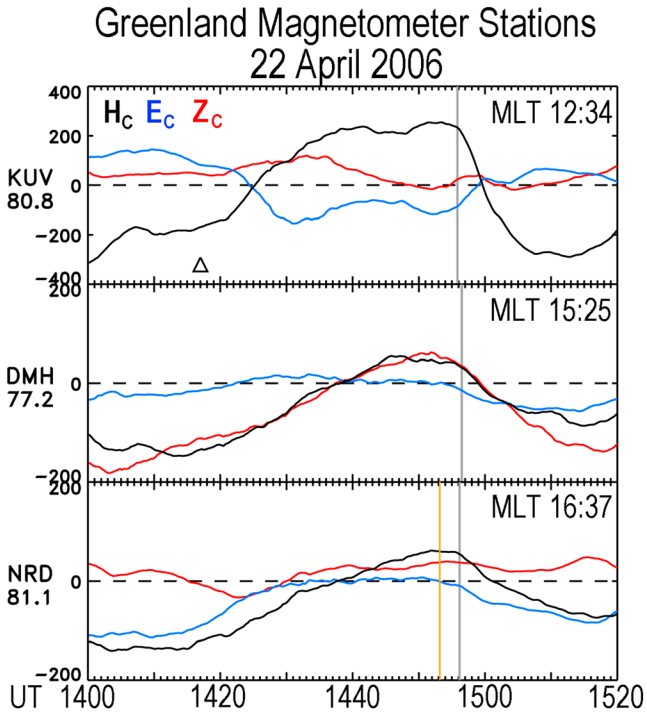

Figure 9. Ground magnetic perturbations observed at DMH and NRD during 1400–1520 UT, and their comparison to the data obtained at KUV (also shown in Figures 4 and 6). (first panel–third panel) The vertical gray line indicates the time for the start of the decrease in the H_C component. The orange line shows the time when DMSP F15 passed directly above NRD.

The upstream part of the sunward flow connects to the tail lobe in which magnetic field lines were convecting toward the lobe reconnection region. When the direction of the IMF changes suddenly, inflow toward the reconnection region would slow down. This causes compression of the magnetic field in the lobe, which propagates backward from the reconnection region. The Alfven speed can be estimated to be roughly 1000 km s^{-1} when the lobe magnetic field and lobe plasma density near the reconnection site are assumed to be 50 nT and 1 cm^{-3}, respectively [*Rosenbauer et al.*, 1975]. The compression wave, which is faster than the Alfven speed, propagates much faster than 1000 km s^{-1}.

When we take 1000 km s^{-1} as a possible lowest value, we can infer that the propagation speed in the ionosphere is roughly 30 km s^{-1}, using a simple convergence factor based on the conservation of magnetic flux. This is determined by the square root of the ratio between the magnetic field magnitudes in the ionosphere and in the tail lobe, which is estimated to be about 30~(50000/50)$^{1/2}$. The speed of more than 30 km s^{-1} in the ionosphere is so fast that substantial time differences would not be detected between two positions a few hundred kilometers apart (i.e., DMH and NRD).

To our knowledge, this study presents the first evidence showing the quasi-instantaneous response of the polar cap sunward flow for positive IMF B_Z. The significance of the compression/rarefaction wave in the magnetosphere and its relation to the ionospheric convection was first pointed out by *Coroniti and Kennel* [1973]. For the IMF southward turning, several previous studies showed that the initial response of the standard two-cell convection is consistent with the propagation of the fast-mode wave [e.g., *Ridley et al.*, 1998; *Nishitani et al.*, 2002; *Lu et al.*, 2002].

5.2. Transition State With a Time Scale of 10–15 Min in the Near-Noon Sector

We have shown that an old convection (or current) system in the near-noon sector is replaced with a new system during 10–15 min. We interpret the ground magnetic variations during this transition state by considering the passage of the main part of the current. The Hall current usually flows at an altitude of around 115 km as a sheet current having an appropriate width. Since a certain type of current-density distribution in the sheet current produces magnetic perturbations that are identical to those produced by a line current [*Kertz*, 1954; *Lühr and Buchert*, 1988], we consider these line current configurations for the interpretation of the ground magnetic variations.

Figures 11a and 11b represent the line current configuration for the explanation of the ground magnetic perturbations for Event A and Event B, respectively. In each case, two half-line currents (bold arrows) exist at a distance of R from G on the ground. The half-line current whose edge is shown with P represents a current associated with old convection, and the other with Q is for new convection. θ_P (or θ_Q) is the angle between GP (or GQ) and the current path. Thin dashed lines are the projection of the path of the half-line currents to the ground.

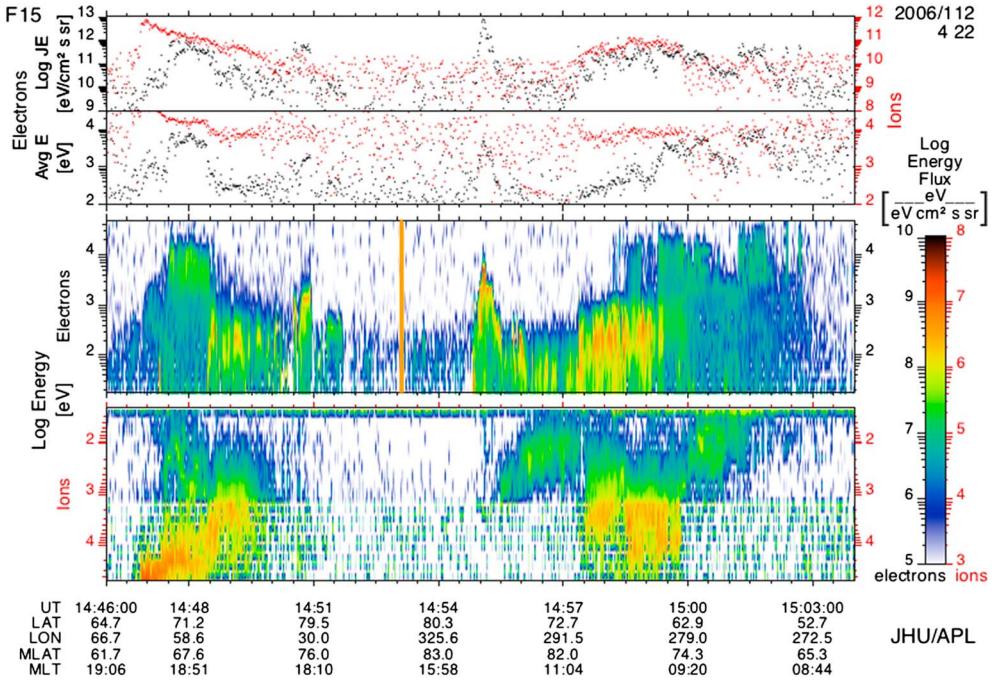

Figure 10. (first panel–fourth panel) Data from the DMSP F15 particle spectrometers. The energy fluxes of the electrons and ions are plotted for the interval 14:46–15:04 UT, with color codes in Figure 10 (third and fourth panels), along with the ion and electron integral energy flux and average energy. The orange line in Figure 10 (third panel) represents the time when DMSP F15 passed directly above NRD.

Naturally, the current continuity requires that the current should not terminate at P or Q. There would be return current. This current also produces some magnetic perturbations at point G. However, in a situation where the main current occurs just above G, the possible contribution from the return current, which is present in a position that is away from the main current, would not exceed the contribution from the main current. It is thus reasonable to introduce the edge of the current for a crude estimation of the magnetic perturbations observed at a certain point on the ground. We consider that this "virtual" edge moves.

From the Biot-Savart law, the magnitude of the magnetic perturbations produced at G by each half-line current can be expressed as

$$B_G = \frac{\mu_0 I}{4\pi R}(1 + \cos\theta) \tag{14}$$

where I is the current strength. Here θ represents θ_P or θ_Q, depending on the line current. We do not consider the coefficient for the conducting Earth here, because the θ dependence in equation (14) is important for our discussion, as is shown below. The line current configuration for $\theta_P = 0°$ and $\theta_Q = 180°$ represents the presence of only a single line current for old convection, and B_G is reduced to $\mu_0 I/(2\pi R)$. In Figure 11a, the line current (with P) produces magnetic perturbations oriented 57° west from north because the direction of the line current is oriented 33° east from north. This direction of the magnetic perturbations reflects the observation at KUV, which was described in section 4.2. In other words, the direction of the line current P is determined so that the produced magnetic perturbation vector at G can be parallel to the observed vector at the beginning of the transition state.

Similarly, the line current configuration for $\theta_P = 180°$ and $\theta_Q = 0°$ represents the presence of only a single line current for new convection. In Figure 11a, the line current (with Q) produces magnetic perturbations oriented 24° west from north because the direction of the line current is oriented 66° east from north. The direction of the line current Q is determined so that the produced magnetic perturbation vector at G can be parallel to the observed vector at the end of the transition state. In Figure 11b, the angles of 70° and 101° reflect the KUV observation in the beginning and end of the transition state for Event B, respectively. As was stated in

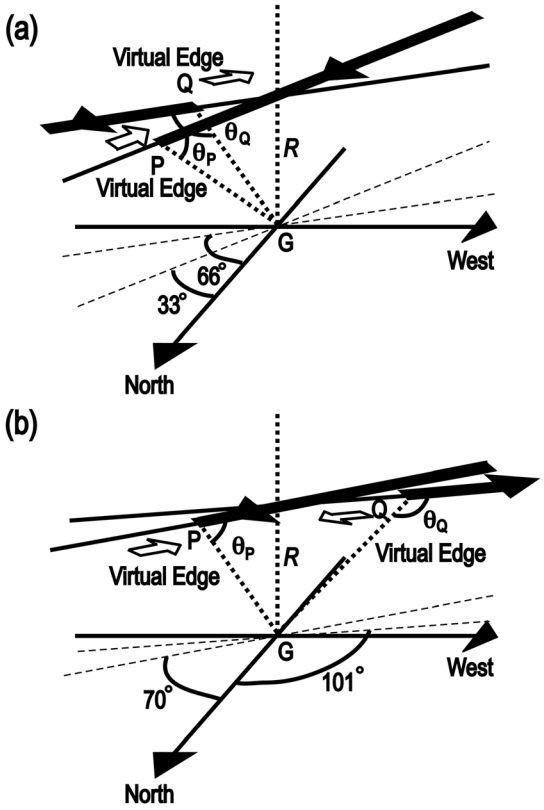

Figure 11. Line current configuration for the explanation of the near-noon ground magnetic perturbations for (a) Event A and (b) Event B. In each illustration, bold arrows indicate two half-line currents flowing at a distance of R from G on the ground. P and Q represent the edge of each half-line current, i.e., the virtual edge. θ_P (or θ_Q) is the angle between GP (or GQ) and the current path.

4.2, the magnetic perturbation at the start and end times was oriented approximately 20° west from north, and 11° east from south, respectively.

When we express $\mu_0 I/(2\pi R)$ from each infinite line current with P or Q as B_P and B_Q, respectively, the northward component (B_H) and the eastward component (B_E) of the magnetic perturbations for arbitrary θ_P and θ_Q, can be shown as follows:

$$B_H = B_P\left(\frac{1+\cos\theta_P}{2}\right)\sin\alpha_P + B_Q\left(\frac{1+\cos\theta_Q}{2}\right)\sin\alpha_Q \quad (15a)$$

$$B_E = B_P\left(\frac{1+\cos\theta_P}{2}\right)\cos(\pi-\alpha_P) + B_Q\left(\frac{1+\cos\theta_Q}{2}\right)\cos(\pi-\alpha_Q) \quad (15b)$$

where (α_P, α_Q) represent (33°, 66°) for Event A, and (70°, −101°) for Event B, respectively.

We consider a situation in which the virtual edge moves with a constant speed. For Event A, the motion of the virtual edge P (open arrow in Figure 11a) reflects that the region of the convection having a strong sunward flow component moves away from the near-noon sector in response to the stop of reconnection with purely northward IMF, and the motion of the virtual edge Q (open arrow in Figure 11a) reflects that the region of the convection toward prenoon approaches the near-noon sector subsequently in response to the start of reconnection with duskward IMF. For Event B, the motion of the virtual edge P (open arrow in Figure 11b) reflects that the region of the clockwise convection moves away from the near-noon sector in response to the stop of reconnection with duskward IMF, and the motion of the virtual edge Q (open arrow in Figure 11b) reflects that new anticlockwise convection approaches the near-noon sector subsequently in response to the start of reconnection with dawnward IMF. For simplicity, we assume that P and Q move with the same speed v, and that both P and Q are located directly above G at $t=0$. The latter assumption assures that the two half-line currents do not intersect each other. We can then express $\cos\theta$ with v, that is,

$$\cos(\pi-\theta_P) = \cos\theta_Q = \frac{vt}{\sqrt{R^2+(vt)^2}} \quad (16)$$

Combined with (15) and (16), the magnetic variations, B_H and B_E, can be shown as a function of time.

In Figures 12a and 12b, we show the calculated magnetic perturbations as a function of time for Event A and B, respectively. For $B_P \sin\alpha_P$ and $B_Q \sin\alpha_Q$ in (15a), we used the values from the KUV H_C component at the start and end of the transition state, respectively. The values from the KUV E_C component at the start and end of the transition state were used for $B_P \cos(\pi-\alpha_P)$ and $B_Q \cos(\pi-\alpha_Q)$ in (15b), respectively. R was assumed to be 115 km.

The three lines in Figures 12a and 12b show the results from the calculation for $v = 0.5$ km s^{-1}, 1 km s^{-1}, and 2 km s^{-1}. The first two velocities represent the situation when the moving speed of the convection region is slower than the local maximum ion drift velocity (i.e., at least ~1.5 km s^{-1}) observed by DMSP F15 or F16.

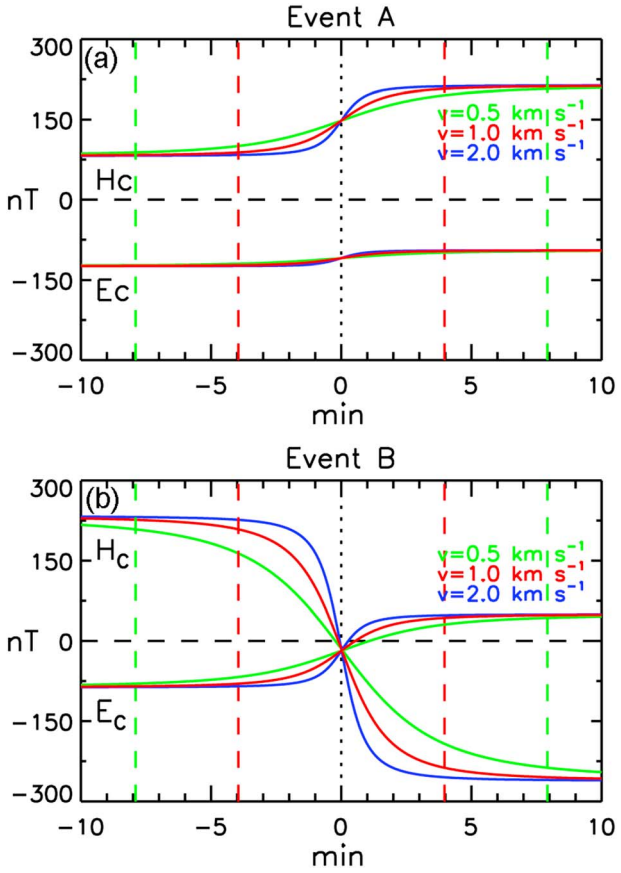

Figure 12. Calculated magnetic perturbations as a function of time for (a) Event A and (b) Event B. The three lines in each panel show the results from the calculation for $v = 0.5$ km s^{-1}, 1 km s^{-1}, and 2 km s^{-1}. Two red dashed lines and green dashed lines show the ranges where 95% of the calculated H_C variation occurs for $v = 1$ km s^{-1} and for $v = 0.5$ km s^{-1}, respectively.

Two red dashed lines and green dashed lines indicate the ranges where 95% of the calculated H_C variation occurs for the case of $v = 1$ km s^{-1} and for the case of $v = 0.5$ km s^{-1}, respectively. For both Event A (Figure 12a) and Event B (Figure 12b), significant magnetic variations appear roughly from −4 min to 4 min for 1 km s^{-1} and roughly from −8 min to 8 min for $v = 0.5$ km s^{-1}. The period of 8–16 min agrees with the duration of the transition state detected in the near-noon sector. On the other hand, for the case of 2 km s^{-1}, the range where 95% of the calculated H_C variation occurs is much shorter than the duration of the transition state detected in the near-noon sector. The transition state detected in the near-noon sector can be interpreted as the approach of a new convection (or Hall current) region to the near-noon sector at the speed of 0.5–1 km s^{-1}, which is coupled with the moving away of the old region, at a similar speed. It appears that the near-noon convection regions are moving slower than the observed local maximum flow.

For Event B (Figures 11b and 12b), the eastward moving virtual edge (Q) with $v = 1$ km s^{-1} would take 25 min to travel ~1500 km. This distance roughly corresponds to the length between 1230 MLT and 1700 MLT along 78° MLAT. It appears that the antisunward flow (i.e., signature of the new convection, blue arrow in Figure 8b) detected at 1700 MLT after only ~13 min (= 1508:54 UT–1456 UT) of the start of the near-noon transition state is not the front of the plasma convection originated from the noon but rather created through a faster process.

In the present paper, we have focused on two events that occurred during a period of positive IMF B_Z and found that the magnetic perturbations in the near-noon sector show a transition with a time scale of 10–15 min. For the response caused by sharp IMF change from negative B_Z to positive B_Z, a transition with a longer period of time may occur. *Clauer and Friis-Christensen* [1988] examined an event for IMF change from negative B_Z to strongly positive B_Z and suggested that the large-scale transition state of currents in the dayside polar cap may occur over a period of 22 min. *Hairston and Heelis* [1995] suggested that the response time for a change in B_Z from negative to positive might be somewhere between 28 and 44 min based on the analysis of DMSP ion drift data. The difference between these response times in the two studies may be due to the difference in the IMF condition. The IMF turned strongly northward with B_Z becoming approximately 20 nT in the event that *Clauer and Friis-Christensen* [1988] examined, while during the interval that *Hairston and Heelis* [1995] investigated there were many reversals in the sign of B_Z, as was explicitly stated in that paper.

6. Conclusions

In this paper, we examined the nature of the transition of the dayside polar cap, which was triggered by fast IMF transitions during a period of positive IMF B_Z. This was done using coordinated observations from a ground magnetometer array and multiple spacecraft. Magnetic perturbation data from three ST5

spacecraft and ion drift data from three DMSP spacecraft were analyzed together with magnetic perturbation data from the Greenland magnetometer array. For the magnetic perturbations from the ST5 spacecraft, we applied a relation of the magnetic perturbations caused by the twin-field-aligned current being antiparallel to the $E \times B$ drift in the northern ionosphere. From our results, we reached the following conclusions:

1. Reverse convection (or related current distribution) in the near-noon sector undergoes a transition state during 10–15 min, responding to a fast IMF change.
2. This near-noon transition state is consistent with the approach of a new convection (or current) region to the near-noon sector at the speed of 0.5–1 km s^{-1}, which is coupled with the moving away of the old convection region at a similar speed. The approach of a new convection region is caused by the start of reconnection with new IMF, and the moving away of the old convection region is caused by the end of reconnection with old IMF. It appears that these convection regions are moving slower than the local maximum flow velocity.
3. For the higher-latitude sunward flow, the convection takes a transition state almost simultaneously (within 1 min) with the near-noon sector, i.e., quasi-instantaneous response. The initial response in the upstream part would be indicated by weakening of the sunward flow. This would be because the lobe convection is weakened by the compression wave launched by the sudden slowdown of the reconnection inflow.

Acknowledgments

S.T. and A.T. thank K. Hosokawa of University of Electro-Communications for his helpful suggestions for the data analysis. Cluster magnetic field data (E. Lucek, PI) are obtained from the ESA Cluster Science Archive. ACE magnetic data (N. Ness, PI) and plasma data (D. McComas, PI) are obtained through the NASA CDAWeb. The DMSP particle detectors were designed by D. Hardy of AFRL, and data are obtained from JHU/APL. The *AL* index was provided by the Data Analysis Center for Geomagnetism and Space Magnetism, Kyoto University.

Alan Rodger thanks the reviewers for their assistance in evaluating the paper.

References

Araki, T., T. Kamei, and T. Iyemori (1984), Polar cap vertical currents associated with northward interplanetary magnetic field, *Geophys. Res. Lett.*, *11*, 23–26, doi:10.1029/GL011i001p00023.

Balogh, A., et al. (2001), The Cluster magnetic field investigation: Overview of in-flight performance and initial results, *Ann. Geophys.*, *19*, 1207–1217.

Clauer, C. R., and E. Friis-Christensen (1988), High-latitude dayside electric fields and currents during strong northward interplanetary magnetic field: Observations and model simulation, *J. Geophys. Res.*, *93*(A4), 2749–2757, doi:10.1029/JA093iA04p02749.

Coroniti, F. V., and C. F. Kennel (1973), Can the ionosphere regulate magnetospheric convection?, *J. Geophys. Res.*, *78*(16), 2837–2851, doi:10.1029/JA078i016p02837.

Cowley, S. W. H., and M. Lockwood (1992), Excitation and decay of solar wind-driven flows in the magnetosphere-ionosphere system, *Ann. Geophys.*, *10*, 103–115.

Etemadi, A., S. W. H. Cowley, M. Lockwood, B. J. I. Bromage, D. M. Willis, and H. Lühr (1988), The dependence of high-latitude dayside ionospheric flows on the north-south component of the IMF: A high time resolution correlation analysis using EISCAT "POLAR" and AMPTE UKS and IRM data, *Planet. Space Sci.*, *36*(5), 471–498, doi:10.1016/0032-0633(88)90107-9.

Fiori, R. A. D., D. H. Boteler, and A. V. Koustov (2012), Response of ionospheric convection to sharp southward IMF turnings inferred from magnetometer and radar data, *J. Geophys. Res.*, *117*, A09302, doi:10.1029/2012JA017755.

Freeman, M. P. (2003), A unified model of the response of ionospheric convection to changes in the interplanetary magnetic field, *J. Geophys. Res.*, *108*(A1), 1024, doi:10.1029/2002JA009385.

Friis-Christensen, E., M. A. McHenry, C. R. Clauer, and S. Vennerstrøm (1988), Ionospheric traveling convection vortices observed near the polar cleft: A triggered response to sudden changes in the solar wind, *Geophys. Res. Lett.*, *15*(3), 253–256, doi:10.1029/GL015i003p00253.

Fukushima, N. (1969), Equivalence in ground geomagnetic effect of Chapman-Vestine's and Birkeland-Alfven's electric current-systems for polar magnetic storms, *Rep. Ionos. Space Res. Jpn.*, *23*(3), 219–227.

Greenspan, M., P. B. Anderson, and J. M. Pelagatti (1988), Characteristics of the thermal plasma monitor (SSIES) for the Defense Meteorological Satellite Program (DMSP) spacecraft S8 through F10 Tech. Rep., AFGL-TR-86-0227, Air Force Geophysical Laboratory, Hanscom Air Force Base, Mass.

Hairston, M. R., and R. A. Heelis (1995), Response time of the polar ionospheric convection pattern to changes in the north-south direction of the IMF, *Geophys. Res. Lett.*, *22*(5), 631–634, doi:10.1029/94GL03385.

Hardy, D. A., L. K. Schmidt, M. S. Gussenhoven, F. J. Marshall, H. C. Yeh, T. L. Shumaker, A. Huber, and J. Pantazis (1984), Precipitating electron and ion detectors (SSJ/4) for block 5D/flights 4-10 DMSP satellites: Calibration and data presentation, Tech. Rep. AFGL-TR-84-0317, Air Force Geophys. Lab., Hanscom Air Force Base, Mass.

Huang, C.-S., D. Murr, G. J. Sofko, W. J. Hughes, and T. Moretto (2000), Ionospheric convection response to changes of interplanetary magnetic field *Bz* component during strong *By* component, *J. Geophys. Res.*, *105*(A3), 5231–5243, doi:10.1029/1999JA000099.

Iijima, T., T. A. Potemra, L. J. Zanetti, and P. F. Bythrow (1984), Large-scale Birkeland currents in the dayside polar region during strongly northward IMF: A new Birkeland current system, *J. Geophys. Res.*, *89*(A9), 7441–7452, doi:10.1029/JA089iA09p07441.

Ishii, M., M. Sugiura, T. Iyemori, and J. A. Slavin (1992), Correlation between magnetic and electric field perturbations in the field-aligned current regions deduced from DE 2 observations, *J. Geophys. Res.*, *97*(A9), 13,877–13,887, doi:10.1029/92JA00110.

Kertz, W. (1954), Modelle für erdmagnetisch induzierte elektrische Ströme im Untergrund, *Nachr. Akad. Wiss. Göttingen, Math.-Phys. Kl. Abt. IIa*, 101–110.

Khan, H., and S. W. H. Cowley (1999), Observations of the response time of high-latitude ionospheric convection to variations in the interplanetary magnetic field using EISCAT and IMP-8 data, *Ann. Geophys.*, *17*, 1306–1335.

Knipp, D. J., et al. (1993), Ionospheric convection response to slow, strong variations in a northward interplanetary magnetic field: A case study for January 14, 1988, *J. Geophys. Res.*, *98*(A11), 19,273–19,292, doi:10.1029/93JA01010.

Laakso, H., C. Perry, S. McCaffrey, D. Herment, A. J. Allen, C. C. Harvey, C. P. Escoubet, C. Gruenberger, M. G. G. T. Taylor, and R. Turner (2010), Cluster active archive: Overview, in *The Cluster Active Archive, Astrophysics and Space Science Proceedings*, edited by H. Laakso et al., pp. 3–37, Springer, Dordrecht, Netherlands.

Le, G., Y. Wang, J. A. Slavin, and R. J. Strangeway (2009), Space Technology 5 multipoint observations of temporal and spatial variability of field-aligned currents, *J. Geophys. Res.*, *114*, A08206, doi:10.1029/2009JA014081.

Luhmann, J. G., R. J. Walker, C. T. Russell, N. U. Crooker, J. R. Spreiter, and S. S. Stahara (1984), Patterns of potential magnetic field merging sites on the dayside magnetopause, *J. Geophys. Res.*, *89*(A3), 1739–1742, doi:10.1029/JA089iA03p01739.

Lühr, H., and S. Buchert (1988), Observational evidence for a link between currents in the geotail and in the auroral ionosphere, *Ann. Geophys.*, *6*(2), 169–176.

Murr, D. L., and W. J. Hughes (2001), Reconfiguration timescales of ionospheric convection, *Geophys. Res. Lett.*, *28*(11), 2145–2148, doi:10.1029/2000GL012765.

Nishitani, N., T. Ogawa, N. Sato, H. Yamagishi, M. Pinnock, J.-P. Villain, G. Sofko, and O. Troshichev (2002), A study of the dusk convection cell's response to an IMF southward turning, *J. Geophys. Res.*, *107*(A3), 1036, doi:10.1029/2001JA900095.

Ridley, A. J., G. Lu, C. R. Clauer, and V. O. Papitashvili (1998), A statistical study of the ionospheric convection response to changing interplanetary magnetic field conditions using the assimilative mapping of ionospheric electrodynamics technique, *J. Geophys. Res.*, *103*(A3), 4023–4039, doi:10.1029/97JA03328.

Rosenbauer, H., H. Grünwaldt, M. D. Montgomery, G. Paschmann, and N. Sckopke (1975), Heos 2 plasma observations in the distant polar magnetosphere: The plasma mantle, *J. Geophys. Res.*, *80*(19), 2723–2737, doi:10.1029/JA080i019p02723.

Ruohoniemi, J. M., and R. A. Greenwald (1998), The response of high-latitude convection to a sudden southward IMF turning, *Geophys. Res. Lett.*, *25*(15), 2913–2916, doi:10.1029/98GL02212.

Slavin, J. A., G. Le, R. J. Strangeway, Y. Wang, S. A. Boardsen, M. B. Moldwin, and H. E. Spence (2008), Space Technology 5 multi-point measurements of near-Earth magnetic fields: Initial results, *Geophys. Res. Lett.*, *35*, L02107, doi:10.1029/2007GL031728.

Sugiura, M., N. C. Maynard, W. H. Farthing, J. P. Heppner, B. G. Ledley, and L. J. Cahill Jr. (1982), Initial results on the correlation between the magnetic and electric fields observed from the DE-2 satellite in the field-aligned current regions, *Geophys. Res. Lett.*, *9*, 985–988, doi:10.1029/GL009i009p00985.

Taguchi, S., and R. A. Hoffman (1995), B_X control of polar cap potential for northward interplanetary magnetic field, *J. Geophys. Res.*, *100*(A10), 19,313–19,320, doi:10.1029/95JA01085.

Taguchi, S., and R. A. Hoffman (1996), Control parameters for polar ionospheric convection patterns during northward interplanetary magnetic field, *Geophys. Res. Lett.*, *23*, 637–640, doi:10.1029/96GL00452.

Taguchi, S., M. Sugiura, J. D. Winningham, and J. A. Slavin (1993), Characterization of the IMF B_Y-dependent field-aligned currents in the cleft region based on DE 2 observations, *J. Geophys. Res.*, *98*, 1393–1407, doi:10.1029/92JA01014.

Taguchi, S., J. A. Slavin, and R. P. Lepping (1997), IMP 8 observations of traveling compression regions in the mid-tail near substorm expansion phase onset, *Geophys. Res. Lett.*, *24*(4), 353–356, doi:10.1029/97GL00121.

Todd, H., S. W. H. Cowley, M. Lockwood, D. M. Willis, and H. Lühr (1988), Response time of the high-latitude dayside ionosphere to sudden changes in the north-south component of the IMF, *Planet. Space Sci.*, *36*(12), 1415–1428, doi:10.1016/0032-0633(88)90008-6.

Wang, Y., G. Le, J. A. Slavin, S. A. Boardsen, and R. J. Strangeway (2009), Space Technology 5 measurements of auroral field-aligned current sheet motion, *Geophys. Res. Lett.*, *36*, L02105, doi:10.1029/2008GL035986.